# Mixed Nanosphere Assemblies at a Liquid–Liquid Interface

Zachary Fink[1,2], Xuefei Wu[2], Paul Y. Kim[2], Alex McGlasson[1], Maged Abdelsamie[2], Todd Emrick[1], Carolin M. Sutter-Fella[3], Paul D. Ashby[3], Brett A. Helms[3], Thomas P. Russell[1,2,4*]

AUTHOR ADDRESS
[1] Department of Polymer Science and Engineering, University of Massachusetts Amherst, Amherst, Massachusetts 01003, USA
[2] Materials Sciences Division, Lawrence Berkeley National Laboratory, Berkeley, California 94720, USA
[3] Molecular Foundry, Lawrence Berkeley National Laboratory, Berkeley, California 94720, USA
[4] Advanced Institute for Materials Research (WPI-AIMR), Tohoku University, 2-1-1 Katahira, Aoba, Sendai 980-8577, Japan

E-mail: russell@mail.pse.umass.edu

Keywords: nanoparticles, liquid interface, adsorption, plasmon resonance, *in situ*, uv-vis reflection spectroscopy

ABSTRACT:

The in-plane packing of gold (Au), polystyrene (PS), and silica ($SiO_2$) spherical nanoparticle (NP) mixtures at a water–oil interface was investigated *in situ* by UV-Vis reflection spectroscopy. All NPs are functionalized with carboxylic acid such that they strongly interact with amine-functionalized ligands dissolved in an immiscible oil phase at the fluid interface. This interaction markedly increases the binding energy of these nanoparticle surfactants (NPSs). The separation distance between the Au NPSs and Au surface coverage are measured by the maximum plasmonic wavelength ($\lambda_{max}$) and integrated intensities as the assemblies saturate for different concentrations of non-plasmonic ($PS/SiO_2$) NPs. As the $PS/SiO_2$ content increases, the time to reach intimate Au NP contact also increases, resulting from their hindered mobility. $\lambda_{max}$ changes within the first few minutes of adsorption due to weak attractive inter-NP forces. Additionally, a sharper peak in the reflection spectrum at NP saturation reveals tighter Au NP packing for assemblies with intermediate non-plasmonic NP content. GISAXS and SEM measurements confirm a decrease in Au NP domain size for mixtures with larger non-plasmonic NP content. The results demonstrate a simple means to

probe interfacial phase separation behavior using *in situ* spectroscopy as interfacial structures densify into jammed, phase-separated NP films.

## 1. Introduction

Liquid interfaces provide a convenient platform to probe fundamental aspects of two-dimensional (2D) colloidal particle assembly. By controlling the in-plane morphology of mixed nanoparticle (NP) assemblies, unique optical, electronic, and mechanical properties[1-3] emerge where functional, large-scale interfacial structures can be generated. Such systems are central to numerous technologies, including emulsion stabilization,[4, 5] nanofiltration membranes,[6] drug delivery,[7, 8] and 3D liquid printing.[9, 10] Noble metal NP assemblies, especially gold (Au), have been of interest since they exhibit coupled surface plasmon resonances characteristic of in-plane NP packing.[11-17] Intrinsic factors, like NP size and shape,[18-20] as well as environmental conditions, such as dielectric media selection,[21, 22] pH,[23] salt concentration,[24] and applied external electric fields[17, 25] have been studied, leading to the development of plasmonic rulers.[26, 27] Furthermore, theoretical arguments, such as the Drude-Lortez approximations[17, 28] for the permittivity of the materials, and the coherent potential approximation[17, 29, 30] for the effective polarizability, have been developed to analyze the resultant data. Nearly all studies have focused on NPs of homogenous shape and composition, while less effort has been directed toward interfaces decorated with mixed NP assemblies. In mixed assemblies, heterogeneous interfaces comprised of well-defined phase-separated domains of different NPs may be produced. Such 2D phase-separated morphologies may open new avenues for fabricating advanced membranes with locally tailorable functions for applications in catalysis,[31] nano-sensors,[32] and nonlinear optics.[33] If these assemblies are on microdroplet or droplet surfaces, the heterogeneous NP distribution produces a new class of liquid “particles” encased by the NPS assembly where the surface functionalization is easily

varied. The way these soft, heterogeneously functionalized NPs assemble is also of rich theoretical interest.[34-36]

Probing the time evolution of NP assemblies at a liquid-liquid interface is challenging, due to the spatial and temporal resolution of the imaging methods, sample damage resulting from high energy sources (x-rays or electrons), or artefacts which can be introduced by invasive probes, *e.g.,* an AFM tip. For densely packed NP mixtures, where in-plane phase separation behavior is of interest, further temporal constraints arise, since the time needed to locate and probe the interface can be long relative to the kinetics of the initial NP adsorption and phase separation. While fluorescence microscopy may be used to image NP laden interfaces, there are several disadvantages when considering the fundamental changes to the NP sturcture via the incorporation of fluorescent tags that need to be placed on the NPs, as well as photobleaching effects from prolonged in situ imaging of the interface. The fluorescent tags can inherently alter the interfacial activity of the NPs through additional interparticle interactions, which will affect the kinetics of the phase separation process, and as a result, the final morphology observed. Furthermore, the initial stages of the assembly may be extremely difficult to capture given the NPs are quite mobile, which will decrease the accuracy of particle localization and thereby reduce the spatiotemporal resolution of the assembly.

UV-Vis reflection spectroscopy on the other hand has proven to be a reliable and rapid tool to characterize the in-plane packing of uniform Au NP assemblies without perturbing the assembly or introducing artefacts.[13, 17, 22-24] Additionally, since Au NPs are inherently plasmonic there is no need to add modifying surface constitusents such as fluourescent tags. As predicted by Mie theory, the plasmon excitation energy depends not only on the properties of individual Au NPs but also on the number of NPs in the ensemble, their relative locations, and interparticle distances.[12, 25, 37] As Au NPs are recruited to the interface and come into

close contact, the local electromagnetic fields between the NPs increase the reflected intensity, which is red shifted by an amount that depends on the interparticle spacing.[17, 26, 38] The increased attractive dipole-dipole interactions for radiation polarized in the plane of the interface causes significant scattering and a phase retardation of the plasmon frequency in the near-field resulting in the red shift.[12, 14] The in-plane NP packing can be characterized by the scattering, absorption, and reflection of light that interacts with individual Au NPs and larger Au NP clusters. Since $SiO_2$ and PS do not have plasmon resonances, any change in the reflection spectrum can be attributed to changes in Au NP packing. We use these characteristics to probe the phase behavior of mixtures of Au NPs with PS and $SiO_2$ NPs at the interface between two immiscible liquids.

We capitalize on prior work using NPSs to form densely packed NP assemblies at the interface between two immiscible liquid phases[10, 39-43] to generate mixed systems comprised of Au, PS, and $SiO_2$ NPs. The formation of NPSs at the fluid interface is driven by electrostatic interactions between oppositely charged carboxylated NPs dispersed in water and aminated polyhedral oligomeric silsesquioxane (POSS) dissolved in silicone oil. This complementary functionality promotes strong NPS binding to the interface and results in jamming when the interfacial area is decreased. To generate the mixed assemblies, Au NPs are mixed with PS or $SiO_2$ NPs and allowed to anchor to the interface. All particles are surface grafted with carboxylic acid terminated ligands to enhance steric repulsion and prevent aggregation in the aqueous phase. Although all the NPs have the same surface functionality, phase separation is induced by capillary forces, depletion interactions,[44-46] and the entropic crystallization of large spheres.[45] To ensure phase separation proceeds, non-plasmonic NPs that are larger than the Au NPs are used, which introduces weak depletion forces and could drive their entropic crystallization. Further, we used different concentrations of Au, PS, or $SiO_2$ NPs in the bulk aqueous phase to control the amount of Au NPs at the fluid interface. We

find that the size difference of the NPs and the number of PS or $SiO_2$ NPs significantly affects the adsorption process and ultimately changes the equilibrium Au NP packing and domain size. *In situ* UV-Vis results were verified using a combination of dynamic interfacial tensiometry, grazing incidence small angle x-ray scattering (GISAXS), and scanning electron microscopy (SEM).

## 2. Results and discussion

### 2.1. NP Adsorption of Mixed NP Assemblies

A planar oil–water interface was prepared in a 20 mm diameter glass vial such that the UV-Vis spectra could be measured during NPs adsorption and rearrangement to form heterogeneous interfacial structures. All experiments were conducted using 14.5 nm Au NPs and mixed with either 15-, 25-, 50-, 100- nm PS NPs or 30 nm $SiO_2$ NPs. Figure 1a shows the system design, where a UV-Vis reflection probe immersed in silicone oil was positioned 3-4 millimeters above the oil–water interface. NP adsorption to the interface begins immediately after POSS-amine is introduced, with a rapid initial adsorption of POSS surfactants followed by diffusion and attachment of the different NPs to the interface. The attachment of both species of NPs to the interface is likely isotropic, given the NP-NP repulsive interactions in the bulk afforded by the negatively charged carboxylate surface functionality. The depletion of NPs in the vicinity of the interface was minimized by increasing the bulk NP concentration. With increasing concentration of non-plasmonic NPs, we hypothesize that the domain size of the phase-separated Au NPs will decrease and that any UV-Vis signal from Au-Au NP plasmons will diminish significantly.

We tuned the concentrations of the plasmonic Au NPs, the non-plasmonic PS and $SiO_2$

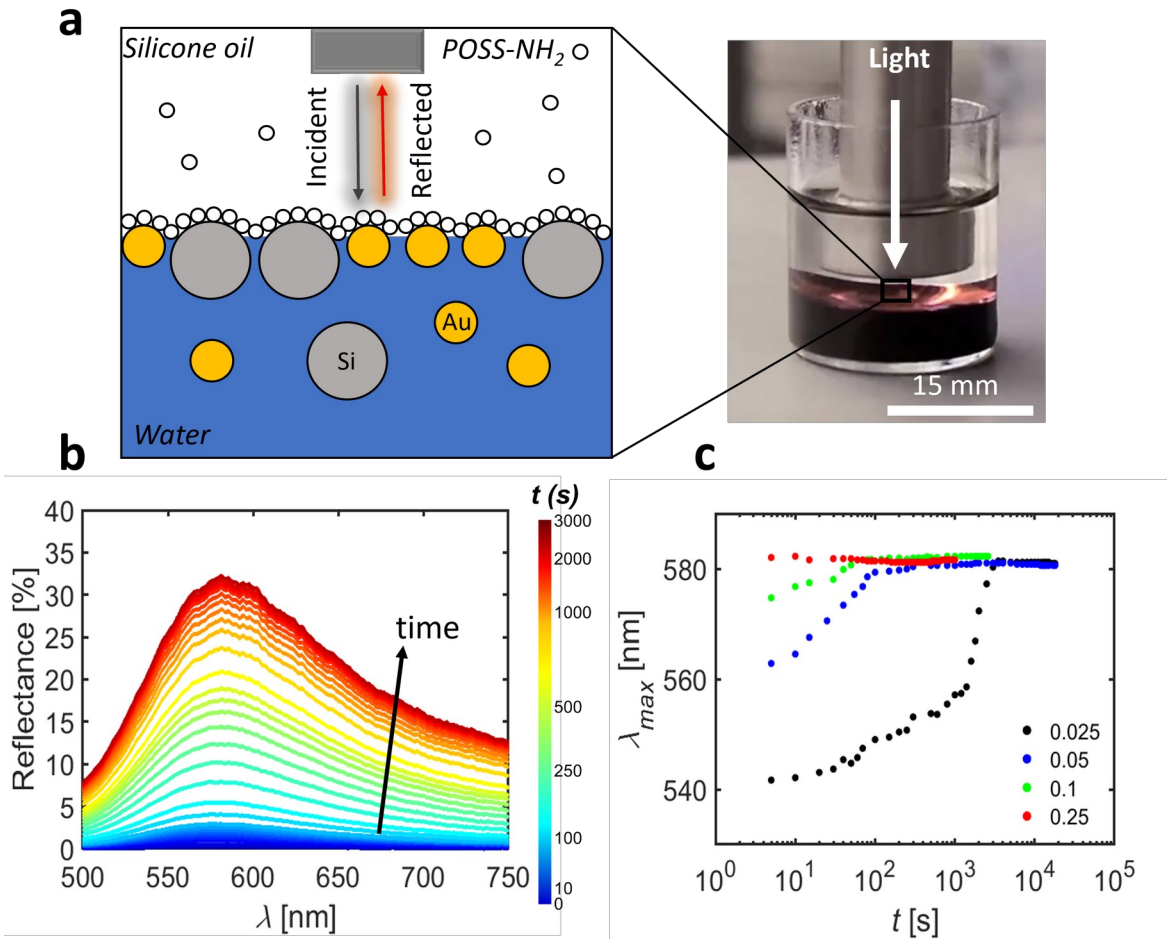


**Figure 1**: UV-Vis reflection set up: (a) picture of the reflection probe immersed in silicone oil normal to the oil–water interface. Only incident light which is back-reflected normal to the probe is collected and analyzed. (b) UV-Vis reflection spectra for a pure Au NP assembly. The reflection intensity increases with time (blue to red color) and is red shifted. (c) POSS concentration dependence on assembly time for pure Au assembly for 0.025, 0.05, 0.1, and 0.25 mg $mL^{-1}$ POSS concentrations.

NPs, and POSS surfactant to obtain complete NP saturation of the interface in a 45-minute period. Prior to any measurement, a silicon wafer was used to generate the reference spectra for the saturated intensity value (100% reflection). Eight NP mixtures were investigated using 25 nm PS NPs with low (0, 0.17), medium (0.24,0.48, 0.66), and high (0.73, 0.79, 0.83) number fractions, $n_{PS}$. Figure 1b shows spectra obtained from a pure Au NP assembly ($n_{PS}$ = 0), while Figure S1 shows the spectra for all other $n_{PS}$. The standard concentration chosen for the oil phase is 0.1 mg $mL^{-1}$ POSS dissolved in 5 centistoke ($mm^2$ $s^{-1}$) silicone oil, though tuning the POSS concentration enables adjustment of the assembly time frames (Figure 1c

and Figure S2). It should be noted that the time increment between measurements is not constant, for visual clarity of the data, and the time between spectra acquisition increases as the assembly proceeds. The spectra at early assembly times, in blue/green, were measured in 3 – 20 second intervals, while the spectra at longer assembly times, in orange/red, were measured in ~500 second intervals. All spectra were obtained by averaging 15 recorded spectra with a 0.01 second acquisition time for each measurement. We modeled each spectrum obtained using the coherent potential approximation (SI Note 1 and Figure S3) in the four-layer stack model, which affords precise determination of the peak position by fitting to a fill factor parameter.[17, 29] The plasmonic nature of the Au NP assemblies allows for the characterization of the interparticle spacing from the wavelength $\lambda$ of the peak position $\lambda_{max}$, percent Au NP surface coverage from the integrated reflectivity, and a qualitative assessment of order from the broadening or narrowing of the data at longer wavelengths.[13, 17, 23, 24, 47]

It is immediately evident in Figure S4 that $n_{PS} = 0$ has significantly higher reflection intensities across all wavelengths than $n_{PS} = 0.83$, indicating that more Au NPs have absorbed to the interface. The peak positions of all the spectra are also red-shifted at longer times as better exemplified by the higher $n_{PS}$. This is more easily visualized by the normalized reflection intensity spectrum, $R/R_o$, where $R$ is the reflectance of any one wavelength and $R_o$ is the reflectance at $\lambda_{max}$, as demonstrated in Figure S5 for all $n_{PS}$. Interestingly, the trend for wavelength broadening/narrowing is not monotonic. Figure S5 shows that the intermediate $n_{PS}$ exhibit a narrowing of the spectra, while the spectra with a high fraction of one component ($n_{PS} = 0$, $n_{PS} = 0.83$) show spectral broadening. This indicates that for mixtures with intermediate $n_{PS}$, the order of the Au NPs within the assemblies increases, while systems with high or very low $n_{PS}$ are more disordered. This may arise from a combination of decreased line tension when local Au domains are surrounded by larger PS NPs,[25, 48] the number of Au NP domain nucleation sites (especially for low $n_{PS}$), as well as any change in

shapes of the larger Au NP assembly structures when small NP clusters eventually coarsen into NP domains. In some measurements, discrete increases in reflection intensity were observed, especially at early times (Figure S6), and may correspond to a coalescence of previously adsorbed Au NPs into small Au NP clusters and further adsorption of Au NPs to the interface. In mixed systems using 30 nm $SiO_2$ NPs, similar results were found, as shown in Figure S7.

The qualitative assessments of Au NP packing for different $n_{PS}$ are supported by quantitative measurements using the coherent approximation model, plasmonic ruler estimations of average Au NP interparticle spacing, and pendant drop tensiometry measurements of each mixture. Interfacial tension (IFT) measurements shown in Figure 2a reflect the NP adsorption over the 45-minute time frame until saturation. The measurements first show a rapid decrease in IFT to 20 mN $m^{-1}$, due to NP adsorption to the interface, followed

by a gradual leveling off as NPSs rearrange, allowing additional NP recruitment to the interface. By fitting the IFT data to a sum of exponentials (Figure S8a) the time scale for adsorption is ~20 seconds and that of rearrangement is about 18 minutes for all mixtures. From the IFT measurements, we estimate the changes in the total packing fraction (PF) of the combined population of NPSs at the oil–water interface over time using equation (1),[49] assuming it is linearly proportional to IFT.

$$PF = \eta \times \frac{\gamma_o - \gamma}{\gamma_o - \gamma_s} \quad (1)$$

Here, $\eta$ is an areal density at saturation ($\sim$84% for a collective 2D jamming of bidisperse disks,[50] $\gamma_o$ is the bare surface tension (43 mN $m^{-1}$), $\gamma$ is the instantaneous IFT, and $\gamma_s$ is the IFT at steady state (4.2 mN $m^{-1}$) for pure Au NPs. The PF time evolution for all the PS-Au NP mixtures is shown in Figure S8b, indicating that the interface is already ~50% populated with

NPs within 20 seconds after the planar interface is formed. The time dependence of the IFT and PF for all the mixtures tested were similar for the first 20 seconds, reflecting the adsorption dominated reduction in IFT, but began to diverge after ~500 seconds, reflecting rearrangement dominated reduction in IFT. IFT, of course, could not distinguish between Au vs PS NP adsorption.

Unlike IFT, UV-Vis reflection characterizes only the Au NPs at the fluid interface. The time required for the peak to shift to the final equilibrium value ($\lambda_{max} \approx 582$ nm) is

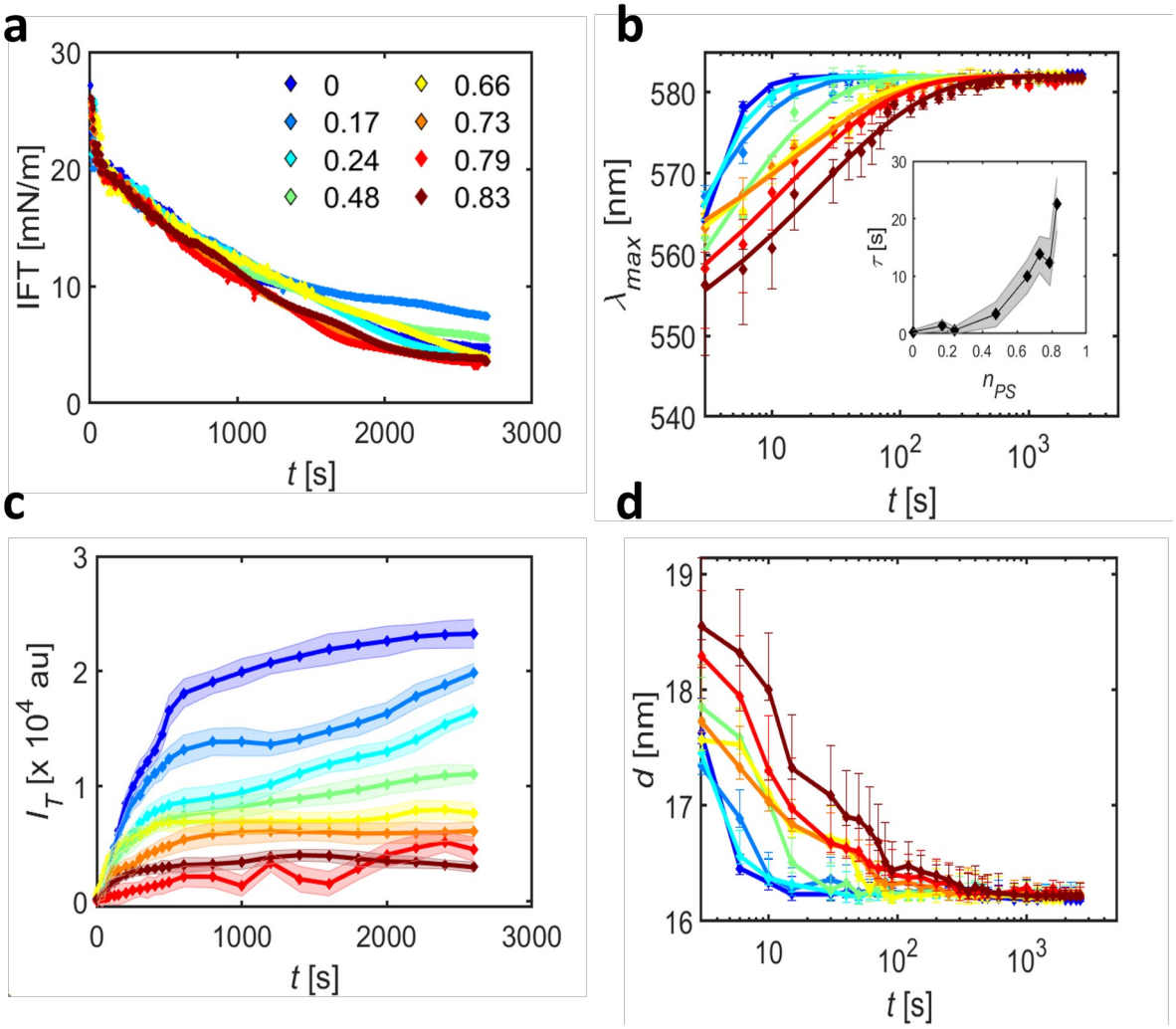


**Figure 2:** Adsorption dynamics of the Au NP population. (a) Interfacial tension data obtained for all mixtures tested using pendant drop tensiometry. (b) $\lambda_{max}$ for each mixture plotted over time measured using UV-Vis reflection spectroscopy as PS concentration increases. (c) Integrated intensity as measured by the summation of intensity for all λ. (d) Interparticle spacing as estimated from Jain *et al.*[26] In all plots ($n_{PS}$ = 0, 0.17, 0.24, 0.48, 0.66, 0.73, 0.79, 0.83) as the color changes from blue to red.

substantially longer for $n_{PS}$ = 0.83 (~800 s) than for $n_{PS}$ = 0 (~20 s) as quantified in Figure 2b for all $n_{PS}$. This indicates that the time to reach intimate Au-Au NP contact increases and the interparticle spacing decreases more slowly in samples with higher $n_{PS}$. This can be attributed to the decrease in Au NP diffusion at the interface resulting from the presence of the larger PS NPs, which isolates the Au NPs, particularly for $n_{PS}$ > 0.5. Additionally, the time evolution of the integrated intensities ($I_T$), a simple summation of the intensity measured for all $\lambda$, as in Figure 2c, can be used to determine the surface coverage of Au NPs over time (Figure S8c). The $I_T$ from a pure Au NP assembly after 45 minutes is used as the saturation intensity, and the instantaneous $I_T$ for all mixtures is divided by this saturation value to estimate Au NP surface coverage. These results confirm that there are more Au NPs at the interface for mixtures with fewer PS NPs in the bulk. Interestingly, the $I_T$ for low and intermediate $n_{PS}$ show a linear increase after ~ 500 seconds, while those for high $n_{PS}$ show a plateau and even a slight decrease in integrated intensity. This suggests that the assembly has already entered a rearrangement-dominated regime, since this transition coincides with the previously presented IFT data. We hypothesize that the behavior in the regime after ~500 seconds may relate to the rate of NP rearrangement and domain coarsening at the interface, which facilitates further NP recruitment to the interfacial area formed. The concentration, size, and number of NP species in the bulk solution determine whether the free space is occupied by an Au or PS NP. Free space generated by a NP rearrangement in high $n_{PS}$ mixtures is more likely filled by PS NPs rather than Au NP, since there is a limited number of Au NPs in the vicinity of the interface. However, since the Au NPs are smaller in diameter, they require less free space to adsorb, and may drive a preference for Au adsorption at longer times, which is seen for low $n_{PS}$ mixtures but not high $n_{PS}$ mixtures. This suggests that for low $n_{PS}$ mixtures the Au NP domain size may increase, and be more ordered, as more Au NPs are integrated into existing Au NP domains at later times.

As shown in the SI, our spectral data can be described by the coherent potential approximation in combination with Drude-Lorentz considerations for the permittivity of the NPs in the assembly. From these fits, we can precisely obtain the wavelength where the reflection intensity reaches $\lambda_{max}$, which corresponds to a preferred separation distance in the assembly. The transition of $\lambda_{max}$ from ~ 560 nm for early assembly times to 582 nm at NPS saturation is evident in Figure 2b. Samples that contain higher $n_{PS}$ take much longer to reach saturation, noting that the greater error associated with the $\lambda_{max}$ value is likely due to inconsistent size and spacing between Au NPs in small Au clusters. It is well known that this change in $\lambda_{max}$ corresponds to the average separation distance between Au NPs and can be fit to decaying exponential functions referred to as plasmon rulers.[26, 27] Plasmon ruler equations have been developed for many systems and are used to determine interparticle spacing from $\lambda_{max}$. Here, we use a universal scaling equation derived by Jain *et al.*:[26]

$$\frac{\Delta\lambda}{\lambda_o} = 0.18\, e^{\frac{-s}{0.23 D_g}} \quad (2)$$

where $\Delta\lambda/\lambda_o$ is the fractional plasmon shift from the single sphere resonance wavelength, $\lambda_o$, $s$ is the average surface-to-surface separation distance, and $D_g$ is the Au NP diameter.[26] Discrete dipole approximation methods have been used to support this empirical equation.[51] With known quantities for $\Delta\lambda/\lambda_o$ and $D_g$, the average center-to-center spacing, $d$, is calculated from $d = s + D_g$. Figure S10 shows $d$ decreasing from 17.6 nm to 16.4 nm for the pure Au NP assembly, and from 18.4 nm to 16.3 nm for $n_{PS}$ = 0.83 as the adsorption time increases. $d$ does not reach the individual NP size, since each NP has an ~1 nm ligand shell.[52] Additionally, NP size dispersity can make the overall NP packing slightly disordered, further contributing to larger $d$ values. In the pure Au NP assembly, the Au NPs almost immediately reach the equilibrium $d$ (~16.3 nm), while the Au NPs in mixtures with higher $n_{PS}$require more time (~500 seconds), but much less than the 2700 seconds for complete interface saturation.

Interestingly, the initial decrease in $d$ is relatively rapid over the first 100 seconds, then decreases more slowly, suggesting the Au NPs form clusters rapidly and that the phase-separated structures begin to grow soon after the initial adsorption (20-50 seconds). To confirm this, the $\lambda_{max}$ plots in Figure 3b were fit to a modified adsorption equation ( $\lambda_{max}=582-b\,e^{-(\frac{t}{\tau})^{1/2}}$ ),[17] where $b$ is a constant and $\tau$ is the characteristic time for the Au NPs to from domains for each mixture. We found that the time to form domains increased with $n_{PS}$, as shown in the inset of Figure S2b. Similar UV-Vis data for the mixtures of Au and 30 nm $SiO_2$ NPs were found regarding the integrated reflectivity, Au NP surface coverage, $\lambda_{max}$ change, change in $d$, and increase in $\tau$ (Figure S9). The Au NP $d$ follows the same trend as the PS NP mixtures but are slightly higher at early times at high $SiO_2$ NP content mixtures due to the increased size of the $SiO_2$ NPs.

Figure 3 illustrates the entire adsorption and rearrangment process, reflecting the observations made from tensiometry and UV-Vis analysis. NPs adsorption uniformly to the oil–water interface, followed by quick dimerization and small cluster formation as a result of the capillary attractions between the NPs. After the adsorption dominated regime, in-plane NP rearrangement and phase separation occurs due to capillary attraction and NP size difference,

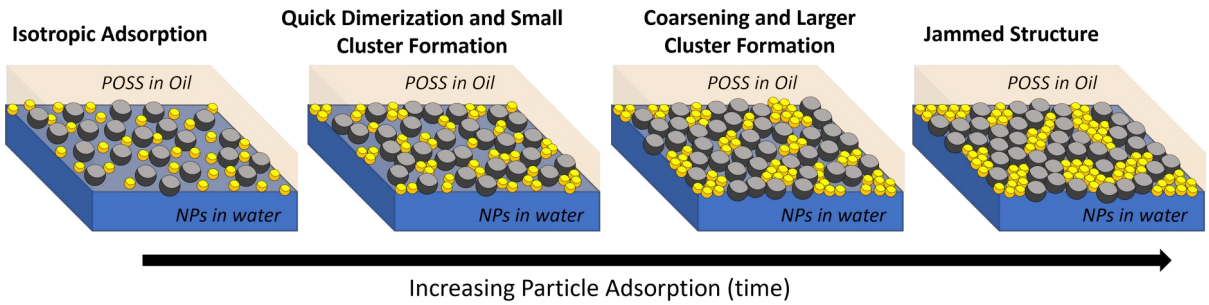


**Figure 3:** Stages of NP adsorption as more NPs are recruited to the interface and phase separate.

which generates depletion forces[44-46]. As more NPs are recruited to the interface, the existing Au NP clusters coarsen into larger Au NP domains. After the interface saturates, NP jamming

prevents further NP adsorption, and generates a stable phase-separated structure (Figure 3 right panel).

The difference in NP size can also greatly affect the assembly kinetics, so 15-, 50-, and 100- nm PS NPs, keeping $n_{PS}$ constant at 0.24, were also analyzed using the UV-Vis reflection spectroscopy. Since the phase separation mechanism relies on the introduction of larger NPs, we expect that the 15 nm PS NPs will behave very differently than the larger PS NPs given the driving force for phase separation is removed. Figure 4 shows how the $I_T$, $\lambda_{max}$, and $d$ change as a function of time for the different PS sizes used in the mixtures. Figure 4a shows $I_T$ initially increase similarly for all PS sizes until ~800 seconds, which reflects the isotropic adsorption of Au NPs. In the rearrangment dominated regime, after ~ 800 seconds, several differences in the rate of change in the $I_T$ are observed. The $I_T$ increases more slowly for smaller PS NPs indicating that the integration of additional Au NPs to the interface is slower, and is consistent with the argument that smaller PS NPs can compete effectively with Au NPs as they require a similar amount of free space to adsorb. However this trend ends abruptly around 1800 and 1200 seconds for 50 and 100 nm respectively, showing decreases in $I_T$. This is explained by the PS NPs displacing the smaller Au NPs given that the energetic gain per particle is much larger for larger NPs.

Figure 4b shows the change in $\lambda_{max}$ for the four sizes of PS tested, and shows a large difference in the behavior of the 15 nm PS vs all larger PS. The smallest PS case shows a much more gradual increase in $\lambda_{max}$ from ~557 nm to 582 nm, where, for example, at 30 seconds registers ~10 nm lower (~570 nm) in $\lambda_{max}$ than all other cases (~580 nm). Further, the

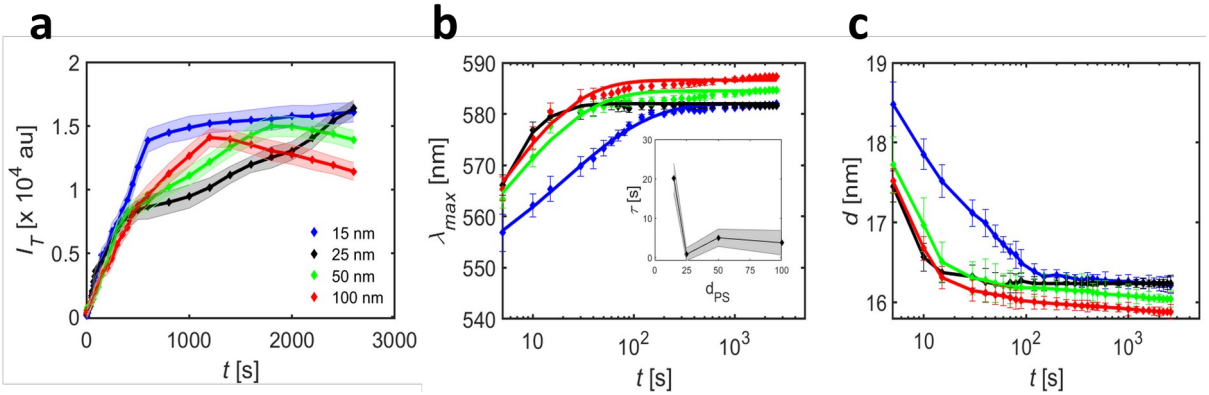


**Figure 4:** Adsorption dynamics of the Au NP population in mixtures with 15-, 25-, 50- and

15 nm PS mixture reaches 582 nm after ~1600 seconds, while all other PS sizes show a more rapid increase in $\lambda_{max}$, all reaching 582 nm within 100 seconds. Since there is no driving force to phase separate, the Au NPs in the 15 nm PS mixture are only pushed together from the increase in areal density. In all other cases, the NPs actively phase separate and come into close contact within ~ 30 seconds. Further, the 50 nm and 100 nm PS NP mixtures reach 584 nm and 587 nm in $\lambda_{max}$, which are higher values than the 582 nm saturation value obtained for both the 15 nm and 25 nm PS NPs. This increase in $\lambda_{max}$ saturation indicates the Au NPs come into even closer contact. These data suggest that the time to form gold clusters is longer for the 15 nm PS NPs and is confirmed by the fit to the adsorption equations using their saturation $\lambda_{max}$ value, where characteristic times decrease from 20 seconds for 15 nm PS NPs to 5 seconds for larger PS NPs (inset Figure 4b). Figure 4c shows the decrease in $d$ from 18.5 nm to 16.2 nm for the 15 nm PS NP assembly, while the decrease in $d$ is much more rapid for the larger PS NP mixtures, as expected from the trend in $\lambda_{max}$. As PS NP size increases the driving force to phase separate also increases and results in closer Au NP $d$ from 16.2 nm to 15.9 nm.

**2.2 Gold Domain Size Determination from GISAXS and SEM**

Although the domain size of the Au NPs could not be determined quantitatively by reflectance measurements, the results suggest that low-to-intermediate packing fractions of non-plasmonic NPs may increase the order within the Au NP domains and generate larger domain sizes than a pure Au NP assembly. Both grazing incidence small angle x-ray scattering (GISAXS) and scanning electron microscopy (SEM) measurements were used to determine the domain sizes of the Au NPs within the jammed assemblies to complement the UV-Vis results. It is important to note that GISAXS includes the scattering from all NP species, but, because of the high electron density of the Au NPs, the signal from the Au NPs dominates the scattering. GISAXS also yields interferences arising from the center-to-center distances between Au NPs that can be compared to the reflectance results. For SEM studies,

the assemblies were prepared on silicon wafers (which may produce artefacts in the assemblies). The obtained images were analyzed using MATLAB® to assess the size and order of the Au NP domains.

2.2.1. *GISAXS*

Planar liquid-liquid interface samples were prepared in 5 mm quartz capillary tubes and the NPs allowed to assemble for 45 minutes prior to GISAXS experiments, which were performed on the 7.3.3 beamline at the Advanced Light Source at Lawrence Berkeley National Laboratory. The oil–water interface was identified by the sharp increase in intensity

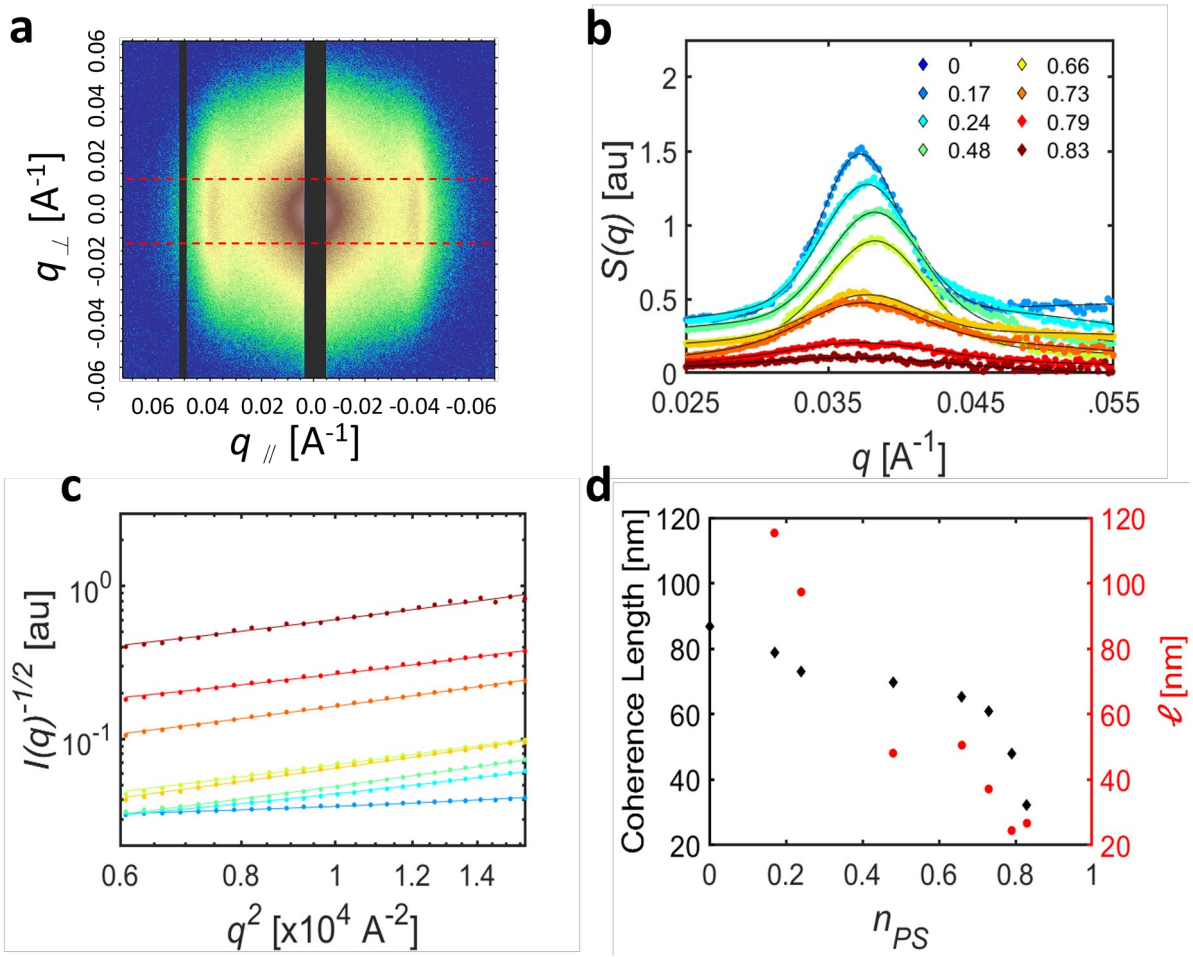


**Figure 5:** GISAXS analysis for domain size characterization. (a) Characteristic 2D GISAXS profile at the oil-water interface. (b) Structure factor for all $n_{PS}$ fit with a gaussian curve to calculate the FWHM for use in the Scherrer analysis. (c) Debye-Bueche plot showing the linear portion of the plot (low $q$) used to calculate the correlation length. (d) Domain size calculations from the Scherrer and Debye-Bueche analyses showing similar trends with a decrease in domain size with increasing $n_{PS}$.

as the beam was scanned from the oil into the water phase (Figure S10). From the measurements, 2D scattering profiles were constructed with the scattering vectors in the plane (parallel, $q_{\parallel}$) or out of the plane (perpendicular, $q_{\perp}$) of the interface. The extension of the scattering normal to the interface, along $q_{\perp}$, results from a truncation of NP packing at the interface and a loss of Fourier components normal to the interface as shown in Figure 5a. Similar characteristics were found for a pure Au NP assembly with 0.025 mg $mL^{-1}$ POSS in silicone oil.[49] Line averaging between -0.013 to 0.013 $q_{\perp}$ converted the 2D profiles to 1D scattering plots. Figure S11 shows the 1D in-plane characterization of the NP assemblies for all $n_{PS}$. The inset of Figure 4a shows the 2D scattering profile characteristic of NPs at the interface. All 1D plots show power law behavior at low $q$, indicative of hierarchical structure formation[53] (*i.e.* Au NP clusters) as well as a distinct maximum in the scattering intensity at $q$ ~ 0.038 $A^{-1}$. The scattering intensities for the highest $n_{PS}$ were weak due to the lower electron density of the PS particles and absorption by the liquid media. The scattering vector at the peak, $q^*$, corresponds to the average interparticle spacing of the NPs assembled at the interface, given by $2\pi/q^*$. Due to NP polydispersity and

the liquid-like nature of the assemblies, the Au NPs exhibit no long-range order within their domains and higher order reflections are absent. Long range order at larger length scales, *i.e.,* cluster to cluster, could not be detected within the $q$-range available. Figure S12 shows the $d$ calculated using $q^*$, which agrees well with that determined by UV-Vis. Interestingly there is a minimum in the interparticle spacing at $n_{PS}$= 0.24. This suggests slightly closer Au NP packing for the intermediate PS compositions, which was similarly observed in UV-Vis.

Using the Scherrer analysis to analyze the peak in the scattering profile, an estimate of the coherence length (crystal size) of the Au NP packing can approximate the average grain size of the Au NP domains.[54, 55] However, the total scattered intensity contribution from the interface, $I(q)$, is a combination of the structure factor, $S(q)$ which reflect lateral organization,

and form factor, *P(q)* which reflects the size and shape of the objects, (*i.e. I(q) = S(q)P(q)*).[56, 57] To accurately calculate the domain size, only the *S(q)* should be used in the Scherrer analysis and can be well approximated by S*(q) = I(q)/P(q)*. Here, *P(q)* is approximated to be the scattering from the bulk solution near the interface and multiplied by a constant. Sample *S(q)* for the pure gold NP assembly is plotted in the inset of Figure S13 from the *I(q)* at the interface and in the bulk, while Figure 5b plots *S(q)* for all $n_{PS}$, focusing at the peak location. Figure 5b clearly shows that the intensity decreases with increasing $n_{PS}$. The domain size is calculated from $D_{SC} = 2\pi K / \beta cos(\Theta)$, where $D_{SC}$ is the coherence length of the ordered Au NP array within a grain, $K$ is a constant (usually ~ 0.9), $\beta$ is the full width at half maximum (FWHM), and $\Theta$ is the scattering angle (~0˚ for grazing incidence). Gaussian curves were fit to each data set in Figure 5b and used to calculate the FWHM. The grain size calculated from the Scherrer analysis is shown in black in Figure 5d. An alternate way to estimate the domain size of a two-phase system is the determination of the Debye-Bueche correlation length, $\xi$.[58] In this model *I(q)* is given by $I(q) \ A/(1+\xi^2 q^2)^2$, and assumes the interface between the domains is sharp with no orientation of the domains. Dividing $\xi$ by the $n_{PS}$will give the chord length, $\ell$, or average size of the Au NP domains. Figure 5c shows Debye-Bueche plots ($I^{-1/2}$ vs $q^2$) where the linear portion of the plot yields the correlation length from the square root of the slope divided by the y-intercept. The domain sizes determined from the Debye-Bueche analysis are shown in red in Figure 5d and follow the same decreasing trend as the coherence lengths determined by the Scherrer analysis. The Scherrer method shows a decrease from 86 nm to 38 nm, while the Debye-Bueche method shows a decrease from ~ 115 to 25 nm. This corresponds to a decrease from roughly 6-8 NP diameters to 2-3 NP diameters. Interestingly the Debye-Bueche method predicts larger domain sizes for the mixtures that have a small $n_{PS}$ than the pure Au NP assembly found using the Scherrer analysis. The increase in domain size

is consistent with the expected increase in order inferred from the UV-Vis reflectance results. In this case, there may be some areas which are locally more ordered for low to intermediate non-plasmonic NP concentrations.

2.2.2. *SEM*

SEM allowed direct visualization of the mixed NP assemblies. $SiO_2$ NPs were used to avoid significant charging by the electron beam from the PS NPs. Like the UV-Vis results, we expect these results to similarly extend to PS NPs. Four samples were prepared: pure Au NP assemblies (0), low $SiO_2$ (0.14), medium $SiO_2$ (0.53), and high $SiO_2$ (0.86) contents like those used for the GISAXS and UV-Vis experiments. SEM samples were prepared on air-plasma treated silicon wafers by depositing ~ 1-2 μL of Au NP/$SiO_2$ NP dispersion followed by covering the entire droplet with a solution of POSS in silicone oil. After the assembly aged for

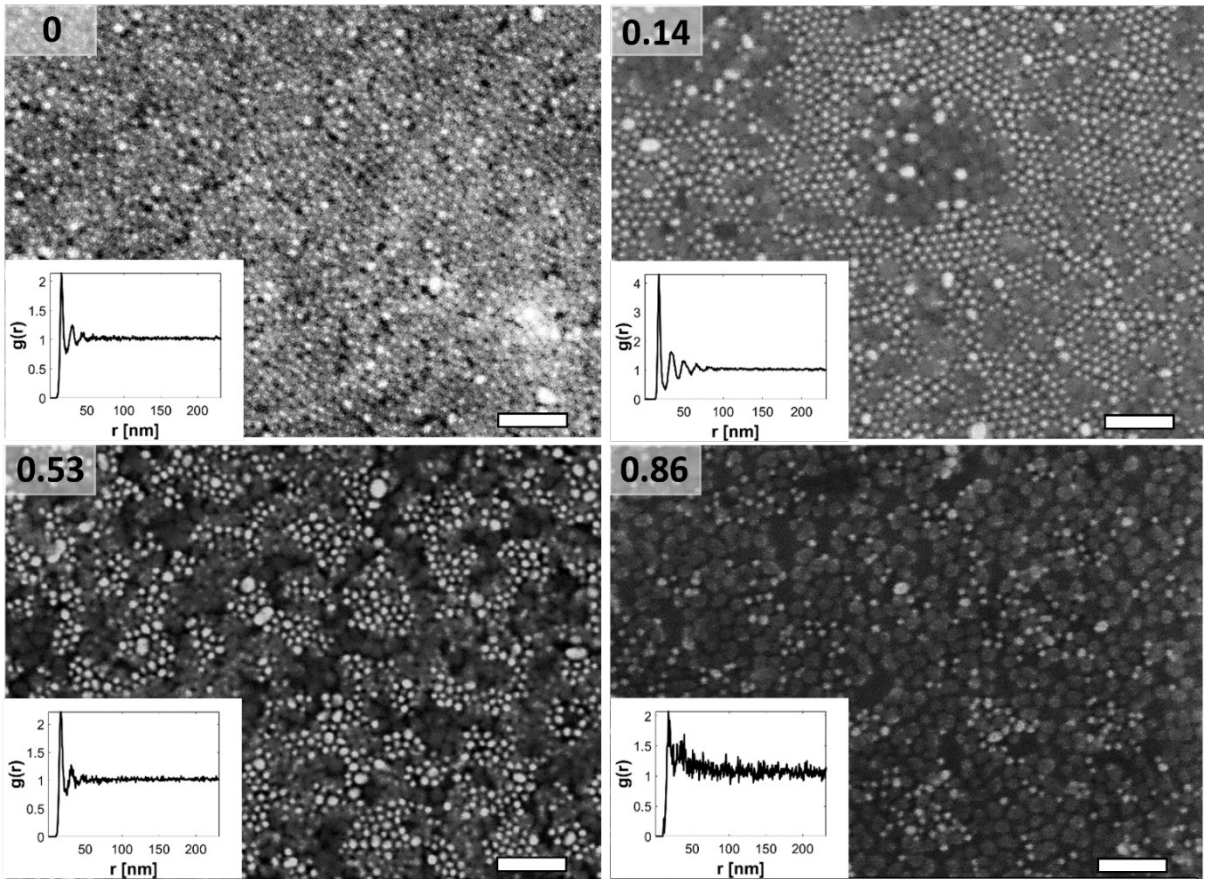


**Figure 6:** SEM images from four different Au/ $SiO_2$ mixtures. All plots are shown with their calculated pair correlation function plotted in the insets. White particles correspond to Au NPs, while grey particles represent $SiO_2$ NPs on a black silicon wafer background. = 0, 0.14, 0.53, 0.86 as indicated in the upper left corner of each image. Scale bars are 100 nm.

45 minutes, toluene was gently infused to slowly remove the nonvolatile silicone oil. The toluene was then allowed to evaporate, and the dried NP assemblies were imaged on the silicon wafers. These assemblies were briefly air-plasma cleaned to remove any organics on the surface and stored under vacuum until SEM analysis. Figure 6 shows the SEM images of the assemblies from the four different mixtures along with the pair correlation function obtained from the images in the inset. From a simple visual observation, several distinct morphologies were identified based on the number of $SiO_2$ NPs in the bulk mixture. These include polycrystalline Au NP domains (Figure 6a), islands of $SiO_2$ NPs in an Au NP matrix (Figure 6b), interpenetrating networks of Au and $SiO_2$ NP domains (Figure S14), islands of Au NP domains in an $SiO_2$ NP matrix (Figure 6c), and small and isolated Au NP clusters in an $SiO_2$ NP matrix (Figure 6d). These morphologies showcase the phase-separated nature of the assemblies and further confirm the close packing of Au NPs with moderate $SiO_2$ NP content.

The spatial correlations of the Au NPs were analyzed using Delaney Triangulation and Voronoi diagrams.[59, 60] From the binarized SEM images, the number of nearest neighbors ($z$), pair correlation functions $g(r)$, and the local hexagonal orientation order parameters $\psi_6$ can all be calculated. Au NPs were isolated in the binarized images by thresholding the intensity and only considering the bright Au NPs. The pair correlation functions in the insets of Figure 6 show peaks that correspond to the nearest neighbor distances and have a value of one when there is no positional correlation. The number of nearest neighbors and pair correlation functions in Figure S15 a and b show some degree of local order, except at high $SiO_2$ fractions, with little long-range order. The Au NP assemblies for the low $SiO_2$ NP fraction (0.14) are more ordered than all the other samples (including the pure Au NP assemblies) with stronger maxima and correlation peaks persisting to larger distances. This supports the observations made by both the UV-Vis and the GISAXS, where the mixtures with low/intermediate $n_{PS}$ showed enhanced Au NP order. The pure Au NP assembly is less

ordered due to the smaller grain sizes that result from an increased number of nucleation sites. In the case of the mixtures, a strong line tension causes a coalescence of smaller Au NP domains into larger Au NP domains. $\psi_6$ gives the degree of local hexagonal order, ranging from zero to one, with zero being complete disorder and one being perfect order corresponding to a single crystal. This can be calculated by equation (3),[61]

$$\psi_6(r_k) = \frac{1}{n_b} \sum_{j \in N_k} e^{6i\theta_{kj}} \quad (3)$$

where $n_b$ is the number of nearest neighbors of particle $k$ at position $r$ and $\theta_{kj}$ is the angle between an arbitrary but fixed axis and the lines connecting the centers of the $n_b$ neighbors and the particle at position $r$. The calculated values of $\psi_6$ for the images obtained are shown in Figure S15c and show that there is a small increase in orientational order for the low $SiO_2$ NP fraction. The domain sizes of the mixtures, shown in Figure S15d, can also be estimated from the spatial correlation function of $\psi_6$ which measures the persistence of hexagonal order and is calculated using equation (4),[46, 60]

$$g_6(r) = \Re\left\{\left\langle \psi_6^{*}(r_k)\,\psi_6(r_j)\right\rangle_{|r_k - r_j| = r}\right\} \quad (4)$$

for pairs of j and k particles. Figure S16 shows the $g_6(r)$, calculated from the images in Figure 6 and are vertically shifted for clarity. The orientational correlation functions show an initial decrease, then plateau near zero which indicates the persistence has ended. The intercept of the plot with the x-axis for each mixture represents an estimation of the domain size, marked by the arrows in Figure S16. From the SEM analysis, it is evident that the domain size for the low $SiO_2$ content is larger than the other mixtures, further supporting the increase in order and domain sizes observed in the UV-Vis and GISAXS experiments.

## 3. Conclusion

While much effort has focused on uniform plasmonic NP assemblies, this work uses mixtures of plasmonic Au NPs and non-plasmonic PS/$SiO_2$ NPs to elucidate phase separation behavior of NP surfactants at a liquid-liquid interface. UV-Vis reflection spectroscopy was used to probe the local optical response of Au NP assemblies, which was confirmed with GISAXS and SEM characterization of the NP assemblies. As the interface saturates with NPs, Au NPs are brought into close contact, leading to an increase in the local surface plasmon resonance, and a redshift of the peak in the reflection spectrum. UV-Vis measurements were performed *in situ* during interface saturation, allowing analysis of the time-evolved Au NP spacing, Au NP surface coverage, and spectral broadening/narrowing. UV-Vis analysis showed that increasing the PS NP fraction decreased the integrated intensity, due to the lower Au NP surface coverage, and delayed the red-shifting of the spectrum, which reflected the prolonged time to form intimate Au NP-Au NP contact. Increased integrated intensity and spectral narrowing at longer times for low and moderate $n_{PS}$ qualitatively suggests a slight increase in order and domain size, although these results could not be quantitively confirmed using UV-Vis. The results indicate that small clusters of 2-3 Au NP form after adsorption, while NP rearrangement opens space to accommodate additional Au NPs to the interface, which are later embedded into existing Au NP domains. The increase in local order and domain size of the Au NP assemblies for low $n_{PS}$arises from an increased probability that the smaller Au NPs will adsorb into available interfacial free as the NPs rearrange. Increasing the size ratio between the PS and Au NPs also had a large effect on the assembly and kinetics, showing a larger and faster decrease in $d$ as compared to PS NPs that were about the same size, and is attributed to the absence of the phase separating driving force.

An increase in domain size and order were also observed by GISAXS and SEM confirming the UV-Vis results. Since relatively high POSS concentrations were used, NPs

were rapidly and irreversibly anchored to the interface, kinetically trapping different phase-separated morphologies that depended on Au NP content. These findings improve our understanding of 2D phase separation of mixed NP surfactant assemblies at fluid-fluid interfaces and are anticipated to open new avenues for fabricating advanced membranes with tunable and locally designed functions for advanced materials applications.

## 4. Experimental Section/Methods

*Nanoparticle Synthesis and POSS Solution Preparation*:

The Au NPs were prepared by a recipe based on the Turkevich method.[62] Briefly, an aqueous solution of hydrogen tetrachloroaurate (Sigma Aldrich, 0.60 mmol) in deionized water (600 mL) was heated to boiling, and stirred vigorously as trisodium citrate (Sigma Aldrich, 60 mL, 2.3 mmol) was quickly added to reduce the gold salt to Au NPs. The solution turned to deep red in few minutes, and after it was cooled to room temperature. After cooling, O-(2-carboxyethyl)-O′-(2-mercaptoethyl)heptaethylene glycol (HS-EG7-COOH, 0.35 mmol purchased from Sigma Aldrich) was added to the solution and stirred overnight in a sealed 1 L flask. The resulting nanoparticles were then washed by centrifugation and redispersed by sonication in deionized water, and was followed by dialysis in DI water for 3 days. The dried Au NPs exhibited a mean diameter of 14.5 ± 3.1nm by TEM particle size analysis with a small fraction of Au NPs almost 25 nm. The bulk Au solution was then diluted to 20 μM with deionized water prior to mixing with non-plasmonic NPs. Bulk solutions 15-, 25-, 50-, and 100- nm PS-COOH NPs were purchased from Microspheres-Nanospheres and bulk solutions of 25 mg $mL^{-1}$ 30 nm $SiO_2$-COOH sicaster® NPs were purchased from Micromod. Both PS and $SiO_2$ NPs were diluted to 1 mg $mL^{-1}$ with deionized water prior to vortex mixing with Au NPs. Various amounts of concentrated non-plasmonic NP solution were then mixed with the

Au NP solution and vortex mixed for 5 minutes to produce well mixed solutions, to prepare the final mixed NP dispersions. A stock solution of 1 mg $mL^{-1}$ POSS ([3-[(2-aminoethyl)amino]propyl]-heptaisobutyl substituted) purchased from Sigma Aldrich in 5 centistoke ($mm^2$ $s^{-1}$) silicone oil (Sigma Aldrich) was prepared by mixing POSS solution in toluene with silicone oil and evaporating off the toluene in a vacuum overnight. The solution was diluted to 0.1 mg $mL^{-1}$ for experiments.

*UV-Vis Measurements*:

Experiments were performed with an RP 22 bifurcated fiber optic reflection/backscatter probe from Thorlabs capable of measuring wavelengths in the 250 – 1200 nm range. The spectrometer leg was connected to a FLAME-T-UV-VIS-ES spectrometer and the source leg was connected to a tungsten halogen source; both were purchased from Ocean Insight Inc. OceanView software was used for all spectra collection. A silicon wafer (CKplas) was used as the refence spectra for the saturated intensity value or 100% reflection prior to all measurements. A planar oil–water interface was prepared in a 2.5 mL glass microbeaker such that the UV-Vis spectra for the assembly could be immediately collected right after interface formation. 1.25 mL of aqueous NP dispersion was loaded into the microbeaker and gently tapped on a flat surface to flatten the interface as much as possible. Sample cells with noticeably large menisci were discarded. The sample cells were then centered under the UV-Vis probe. To prevent a change in curvature after the silicone oil solution was placed on top of the water, a small amount of oil with no ligand was added on top of water and the UV-Vis reflection probe was placed around 3-4 millimeters above the oil–water interface. This was where the maximum intensity was achieved and resulted in 1-2 $mm^2$ sample illumination area. 1 mL POSS solution was then carefully added on top of the aqueous NP dispersion so as to not perturb the interface. Spectra were immediately collected

after interface generation where one spectrum consisted of 15 averaged measurements in the normal incident back reflection geometry. All spectra which were subsequently processed in MATLAB®.

*GISAXS Procedure*:

Grazing incidence scattering experiments were performed at the Advanced Light Source (ALS) at Lawrence Berkeley National Laboratory on beamline 7.3.3 using a 10 keV x-ray beam and measurable $q$ range from 0.004 to 3.5 $A^{-1}$. Samples were prepared in 5 mm quartz capillary tubes with 0.01 mm wall thickness in a similar manner to that used for the bilayer sample preparation for the reflection measurements. The interface was carefully prepared by filling the capillaries first by the NP dispersion followed by the POSS solution to the top. Samples were left to age for ~45 minutes prior to loading the sample into the beam. To locate the interface, the beam was scanned from oil to the aqueous phase, where the interface was identified by finding a sharp increase in transmission intensity. The beam position was then moved slightly into the oil phase to prevent significant scattering from the bulk aqueous phase. Once the interface was located, the sample was exposed to the beam for 20 seconds to obtain the 2D scattering plot. The large scattering contrast between the Au NPs and all other components in the system lead to strong Au scattering from the interface. 2D scattering profiles reveal extended scattering intensity normal to the interface. In-plane characterization of the profiles by horizontal averaging between -0.013 to 0.013 $q_{\perp}$ reveals scattering maxima at $q$ values related to the interparticle spacing. Domain size calculations were done through both Scherrer and Debye-Bueche analyses. Peak isolation for the Scherrer analysis was done dividing the form factor and replotted in the peak range (0.025-0.055 $A^{-1}$).

*SEM Imaging*:

Scanning electron microscopy (SEM) was conducted using a Zeiss ULTRA 55 - FESEM and 5 kV accelerating voltage to collect images of the dried films. SEM samples were prepared on air-plasma treated silicon wafers using a Harrick Plasma PDC-001 plasma cleaner by depositing ~ 1-2 μL drop of diluted Au/ $SiO_2$ solution followed by covering the entire drop with the POSS silicone oil solution. The NPs were allowed to assemble for at least 45 minutes prior to gentle toluene infusion to slowly remove the nonvolatile silicone oil. After toluene evaporation, dried NP films were observed on the silicon wafers and were briefly air-plasma cleaned and stored under vacuum until SEM analysis. All image analysis was done using image processing from the MATLAB® image processing toolkit. The raw grayscale images were filtered with a Gaussian blur to reduce noise and then converted to a binary image by thresholding. Only Au particles were considered in the analysis, so the thresholding was done such that areas that contained Au particles were white (1) and areas that had no particles or $SiO_2$ particles were black (0). White pixels were grouped together with a minimum size and discarded as noise if below that minimum size. The centroids of the grouped pixels (particles) were calculated from pixel locations. Software obtained from Kim *et al.*[60, 63] was used to analyze the packing structures of the mixed NP assemblies in MATLAB® to obtain the number of nearest neighbors ($z$), pair correlation functions $g(r)$, the local hexagonal orientation order parameters $\psi_6$, and the spatial correlation function of $\psi_6$, $g_6(r)$.

**Supporting Information**

Supporting Information is available from the Wiley Online Library or from the author. Text describes the coherent potential approximation and four-layer stack model used in determining the theoretical optical response. A brief description of the Drude-Loretz model is provided for the calculation of permittivity followed by the description for polarizability of

individual NPs and NPs in a monolayer assembly. Figure S1, reflection profiles for all Au, PS mixtures tested Figure S2, reflection profiles for pure gold assemblies using four different POSS concentrations tested and their associated peak normalized profiles; Figure S3, Coherent potential approximation four layer stack schematic with the plots for permittivity and polarizability, as well as the theoretical and experimental reflectance for pure gold; Figure S4, reflection profiles for pure gold assembly and $n_{PS}$ = 0.83; Figure S5, peak normalized profiles from Figure S3 for all Au, PS mixtures tested; Figure S6, reflection profile showing a step increase in reflectance at an early time; Figure S7, reflection profiles for four different $SiO_2$ mixtures with their associated peak normalized profiles; Figure S8, interfacial tension results for all Au, PS mixtures with fits for a sum of exponentials and packing fraction and gold surface coverage; Figure S9, adsorption dynamics, gold coverage, and interparticle spacing for all Au, $SiO_2$ mixtures tested; Figure S10, 1D GISAXS scattering profiles for locating the interface as the beam moves from the oil to the water phase with associated 2D profiles; Figure S11, all 1D scattering profiles at the interface for all Au, PS mixtures; Figure S12, interparticle spacing as measured using GISAXS; Figure S13, S(q) calculation and peak isolation for the Scherrer analysis; Figure S14, SEM image of an interpenetrated Au, $SiO_2$ morphology; Figure S15, SEM analysis in terms of $z$, $g(r)$, $\psi_6$, and $g_6(r)$; Figure S16, $g_6(r)$ vertically shifted for easy comparison of the estimated domain sizes.

**Acknowledgements:**

This work supported by the U.S. Department of Energy, Office of Science, Office of Basic Energy Sciences, Materials Sciences and Engineering Division under Contract No. DE-AC02-05-CH11231 within the Adaptive Interfacial Assemblies Towards Structuring Liquids program (KCTR16). This work was done in collaboration with Lawrence Berkeley National

Lab at the Advanced Light Source beamline 7.3.3 and supported by the NSF and the DOE SCGSR Program. M.A. acknowledges support by the US Department of Energy, Office of Science, Office of Basic Energy Sciences, Materials Sciences and Engineering Division under Contract No. DE-AC02-05-CH11231 (D2S2 program KCD2S2). Work at the Molecular Foundry was supported by the Office of Science, Office of Basic Energy Sciences, of the U.S. Department of Energy under Contract No. DE-AC02-05CH11231 and is gratefully acknowledged by C.M.S.-F. We also acknowledge support from NSF-CBET (NSF-2136955) Structural Control at Fluidic Interfaces with Nanoparticle Surfactant Assemblies.

**Conflict of Interest:**

The authors declare no conflict of interest.

Received: ((will be filled in by the editorial staff))
Revised: ((will be filled in by the editorial staff))
Published online: ((will be filled in by the editorial staff))

**References:**

[1] Bresme, F.; Oettel, M. Nanoparticles at Fluid Interfaces. *J Phys.:Condens. Matter* **2007**, 19, DOI: 10.1088/0953-8984/19/41/413101.

[2] Forth, J.; Mariano, A.; Chai, Y.; Toor, A.; Hasnain, J.; Jiang, Y. F.; Feng, W. Q.; Liu, X. B.; Geissler, P. L.; Menon, N.; Hemls, B. A.; Ashby, P. D.; Russell, T. P.; The Buckling Spectra of Nanoparticle Surfactant Assemblies. *Nano Lett.* **2021**, 21, 7116-7122, DOI: 10.1021/acs.nanolett.1c01454.

3] Tang, Z. Y.; Kotov, N. A. One-Dimensional Assemblies of Nanoparticles: Preparation, Properties, and Promise. *Adv. Mater.* **2005**, 17, 951-962, DOI: 10.1002/adma.200401593 24.

[4] Sullivan, A. P.; Kilpatrick, P. K. The Effects of Inorganic Solid Particles on Water and Crude Oil Emulsion Stability. *Ind. Eng. Chem. Res.* **2002**, 41, 3389-3404, DOI: 10.1021/ie010927n.

[5] van der Sman, R. G. M.; van der Goot, A. J. The Science of Food Structuring. *Soft Matter* **2009**, 5, 501-510, DOI: 10.1039/b718952b.

[6] Lv, Y.; Du, Y.; Qiu, W. Z.; Xu, Z. K. Nanocomposite Membranes Via the Codeposition of Polydopamine/Polyethylenimine with Silica Nanoparticles for

Enhanced Mechanical Strength and High Water Permeability. *ACS Appl. Mater. Interfaces* **2017**, 9, 2966- 2972, DOI: 10.1021/acsami.6b13761.

[7] Dinsmore, A. D.; Hsu, M. F.; Nikolaides, M. G.; Marquez, M.; Bausch, A. R.; Weitz, D. A. Colloidosomes: Selectively Permeable Capsules Composed of Colloidal Particles. *Science* **2002**, 298, 1006-1009, DOI: 10.1126/science.1074868.

[8] Strong, L. E.; West, J. L. Thermally Responsive Polymer-Nanoparticle Composites for Biomedical Applications. *Wiley Interdiscip. Rev.: Nanomed. Nanobiotechnol.* **2011**, 3, 307-317, DOI: 10.1002/wnan.138.

[9] Haase, M. F.; Stebe, K. J.; Lee, D. Continuous Fabrication of Hierarchical and Asymmetric Bijel Microparticles, Fibers, and Membranes by Solvent Transfer-Induced Phase Separation (Strips). *Adv. Mater.* **2015**, 27, 7065-7071, DOI: 10.1002/adma.201503509.

[10] Cain, J. D.; Azizi, A.; Maleski, K.; Anasori, B.; Glazer, E. C.; Kim, P. Y.; Gogotsi, Y.; Helms, B. A.; Russell, T. P.; Zettl, A. Sculpting Liquids with Two-Dimensional Materials: The Assembly of Ti3c2tx Mxene Sheets at Liquid Liquid Interfaces. *ACS Nano* **2019**, 13, 12385-12392, DOI: 10.1021/acsnano.9b05088.

[11] Aravind, P. K.; Nitzan, A.; Metiu, H. The Interaction between Electromagnetic Resonances and Its Role in Spectroscopic Studies of Molecules Adsorbed on Colloidal Particles or Metal Spheres. *Surf. Sci.* **1981**, 110, 189-204, DOI: 10.1016/0039-6028(81)90595-1.

[12] Elbahri, M.; Homaeigohar, S.; Assad, M. A. Reflective Coloration from Structural Plasmonic to Disordered Polarizonic. *Adv. Photonics Res.* **2021**, 2, DOI: 10.1002/adpr.202100009.

[13] Fang, P. P.; Chen, S.; Deng, H. Q.; Scanlon, M. D.; Gumy, F.; Lee, H. J.; Momotenko, D.; Amstutz, V.; Cortes-Salazar, F.; Pereira, C. M.; Yang, Z.; Girault, H. H. Conductive Gold Nanoparticle Mirrors at Liquid/Liquid Interfaces. *ACS Nano* **2013**, 7, 9241-9248, DOI: 10.1021/nn403879g.

[14] Halas, N. J.; Lal, S.; Chang, W. S.; Link, S.; Nordlander, P. Plasmons in Strongly Coupled Metallic Nanostructures. *Chem. Rev.* **2011**, 111, 3913-3961, DOI: 10.1021/cr200061k.

[15] Lalander, C. H.; Zheng, Y.; Dhuey, S.; Cabrini, S.; Bach, U. DNA-Directed Self-Assembly of Gold Nanoparticles onto Nanopatterned Surfaces: Controlled Placement of Individual Nanoparticles into Regular Arrays. *ACS Nano* **2010**, 4, 6153-6161, DOI: 10.1021/nn101431k.

[16] Ma, Y.; Zagar, C.; Klemme, D. J.; Sikdar, D.; Velleman, L.; Montelongo, Y.; Oh, S. H.; Kucernak, A. R.; Edel, J. B.; Kornyshev, A. A. A Tunable Nanoplasmonic Mirror at an Electrochemical Interface. *ACS Photonics* **2018**, 5, 4604-4616, DOI: 10.1021/acsphotonics.8b01105.

[17] Montelongo, Y.; Sikdar, D.; Ma, Y.; McIntosh, A. J. S.; Velleman, L.; Kucernak, A. R.; Edel, J. B.; Kornyshev, A. A. Electrotunable Nanoplasmonic Liquid Mirror. *Nat. Mater.* **2017**, 16, 1127-1135, DOI: 10.1038/Nmat4969.

[18] Giannini, V.; Fernandez-Dominguez, A. I.; Sonnefraud, Y.; Roschuk, T.; Fernandez-Garcia, R.; Maier, S. A. Controlling Light Localization and Light-Matter Interactions with Nanoplasmonics. *Small* **2010**, 6, 2498-2507, DOI: 10.1002/smll.201001044 25.

[19] Yang, A.; Hryn, A. J.; Bourgeois, M. R.; Lee, W. K.; Hu, J.; Schatz, G. C.; Odom, T. W. Programmable and Reversible Plasmon Mode Engineering. *Proc. Natl. Acad. Sci. U. S. A.* **2016**, 113, 14201-14206, DOI: 10.1073/pnas.1615281113.

[20] Yan, B.; Boriskina, S. V.; Reinhard, B. M. Optimizing Gold Nanoparticle Cluster Configurations (N <= 7) for Array Applications. *J. Phys. Chem. C* **2011**, 115, 4578-4583, DOI: 10.1021/jp112146d.

[21] Kinnan, M. K.; Chumanov, G. Plasmon Coupling in Two-Dimensional Arrays of Silver Nanoparticles: II. Effect of the Particle Size and Interparticle Distance. *J. Phys. Chem. C* **2010**, 114, 7496-7501, DOI: 10.1021/jp911411x.

[22] Smirnov, E.; Peljo, P.; Scanlon, M. D.; Gumy, F.; Girault, H. H. Self-Healing Gold Mirrors and Filters at Liquid-Liquid Interfaces. *Nanoscale* **2016**, 8, 7723-7737, DOI: 10.1039/c6nr00371k.

[23] Turek, V. A.; Cecchini, M. P.; Paget, J.; Kucernak, A. R.; Kornyshev, A. A.; Edel, J. B. Plasmonic Ruler at the Liquid-Liquid Interface. *ACS Nano* **2012**, 6, 7789-7799, DOI: 10.1021/nn302941k.

[24] Velleman, L.; Sikdar, D.; Turek, V. A.; Kucernak, A. R.; Roser, S. J.; Kornyshev, A. A.; Edel, J. B. Tuneable 2D Self-Assembly of Plasmonic Nanoparticles at Liquid| Liquid Interfaces. *Nanoscale* **2016**, 8, 19229-19241, DOI: 10.1039/c6nr05081f.

[25] Scanlon, M. D.; Smirnov, E.; Stockmann, T. J.; Peljo, P. Gold Nanofilms at Liquid-Liquid Interfaces: An Emerging Platform for Redox Electrocatalysis, Nanoplasmonic Sensors, and Electrovariable Optics. *Chem. Rev.* **2018**, 118, 3722-3751, DOI: 10.1021/acs.chemrev.7b00595.

[26] Jain, P. K.; Huang, W. Y.; El-Sayed, M. A. On the Universal Scaling Behavior of the Distance Decay of Plasmon Coupling in Metal Nanoparticle Pairs: A Plasmon Ruler Equation. *Nano Lett.* **2007**, 7, 2080-2088, DOI: 10.1021/nl071008a.

[27] Kelesidis, G. A.; Gao, D.; Starsich, F. H. L.; Pratsinis, S. E. Light Extinction by Agglomerates of Gold Nanoparticles: A Plasmon Ruler for Sub-10 nm Interparticle Distances. *Anal. Chem.* **2022**, 94, 5310-5316, DOI: 10.1021/acs.analchem.1c05145.

[28] Alabastri, A.; Tuccio, S.; Giugni, A.; Toma, A.; Liberale, C.; Das, G.; De Angelis, F.; Di Fabrizio, E.; Zaccaria, R. P. Molding of Plasmonic Resonances in Metallic Nanostructures: Dependence of the Non-Linear Electric Permittivity on System Size and Temperature. *Materials* **2013**, 6, 4879-4910, DOI: 10.3390/ma6114879.

[29] Persson, B. N. J.; Liebsch, A. Optical-Properties of Two-Dimensional Systems of Randomly Distributed Particles. *Phys. Rev. B* **1983**, 28, 4247-4254, DOI: 10.1103/PhysRevB.28.4247.

[30] Sikdar, D.; Kornyshev, A. A. Theory of Tailorable Optical Response of Two-Dimensional Arrays of Plasmonic Nanoparticles at Dielectric Interfaces. *Sci. Rep.* **2016**, 6, DOI: 10.1038/srep33712.

[31] Wang, D.; Liu, J.; Xi, J. B.; Jiang, J. Z.; Bai, Z. W. Pd-Fe Dual-Metal Nanoparticles Confined in the Interface of Carbon Nanotubes/N-Doped Carbon for Excellent Catalytic Performance. *Appl. Surf. Sci.* **2019**, 489, 477-484, DOI: 10.1016/j.apsusc.2019.06.039.

[32] Koh, C. R. E. L.; Sim, O. W. R. Y. F.; Leong, S. X.; Boong, S. K.; Chong, C. R. C.; Ling, X. Y. Plasmonic Nanoparticle-Metal-Organic Framework (Np-Mof) Nanohybrid Platforms for Emerging Plasmonic Applications. *ACS Mater. Lett.* **2021**, 3, 557-573, DOI: 10.1021/acsmaterialslett.1c00047.

[33] Kityk, I. V.; Ebothe, J.; Fuks-Janczarek, I.; Umar, A. A.; Kobayashi, K.; Oyama, M.; Sahraoui, B. Nonlinear Optical Properties of Au Nanoparticles on Indium-Tin Oxide Substrate. *Nanotechnology* **2005**, 16, 1687-1692, DOI: 10.1088/0957-4484/16/9/046.

[34] Bianchi, E.; Likos, C. N.; Kahl, G. Self-Assembly of Heterogeneously Charged Particles under Confinement. *ACS Nano* **2013**, 7, 4657-4667, DOI: 10.1021/nn401487m 26.

[35] Morphew, D.; Shaw, J.; Avins, C.; Chakrabarti, D. Programming Hierarchical Self-Assembly of Patchy Particles into Colloidal Crystals Via Colloidal Molecules. *ACS Nano* **2018**, 12, 2355-2364, DOI: 10.1021/acsnano.7b07633.

[36] Zhang, Z. L.; Glotzer, S. C. Self-Assembly of Patchy Particles. *Nano Lett.* **2004**, 4, 1407-1413, DOI: 10.1021/nl0493500.

[37] Kelly, K. L.; Coronado, E.; Zhao, L. L.; Schatz, G. C. The Optical Properties of Metal Nanoparticles: The Influence of Size, Shape, and Dielectric Environment. *J. Phys. Chem. B* **2003**, 107, 668-677, DOI: 10.1021/jp026731y.

[38] Dusemund, B.; Hoffmann, A.; Salzmann, T.; Kreibig, U.; Schmid, G. Cluster Matter - the Transition of Optical Elastic-Scattering to Regular Reflection. Z. Phys. D: *At., Mol. Clustrs* **1991**, 20, 305-308, DOI 10.1007/Bf01543997.

[39] Chai, Y.; Lukito, A.; Jiang, Y. F.; Ashby, P. D.; Russell, T. P. Fine-Tuning Nanoparticle Packing at Water-Oil Interfaces Using Ionic Strength. *Nano Lett.* **2017**, 17, 6453-6457, DOI: 10.1021/acs.nanolett.7b03462.

[40] Cui, M. M.; Emrick, T.; Russell, T. P. Stabilizing Liquid Drops in Nonequilibrium Shapes by the Interfacial Jamming of Nanoparticles. *Science* **2013**, 342, 460-463, DOI: 10.1126/science.1242852.

[41] Gu, P. Y.; Kim, P. Y.; Chai, Y.; Ashby, P. D.; Xu, Q. F.; Liu, F.; Chen, Q.; Lu, J. M.; Russell, T. P. Visualizing Assembly Dynamics of All-Liquid 3d Architectures. *Small* **2022**, 18, DOI: 10.1002/smll.202105017.

[42] Shi, S. W.; Russell, T. P. Nanoparticle Assembly at Liquid-Liquid Interfaces: From the Nanoscale to Mesoscale. *Adv. Mater.* **2018**, 30, DOI: 10.1002/adma.201800714.

[43] Toor, A.; Feng, T.; Russell, T. P. Self-Assembly of Nanomaterials at Fluid Interfaces. *Eur. Phys. J. E.* **2016**, 39, DOI: 10.1140/epje/i2016-16057-x.

[44] Baranov, D.; Fiore, A.; van Huis, M.; Giannini, C.; Falqui, A.; Lafont, U.; Zandbergen, H.; Zanella, M.; Cingolani, R.; Manna, L. Assembly of Colloidal Semiconductor Nanorods in Solution by Depletion Attraction. *Nano Lett.* **2010**, *10*, 743-749, DOI: 10.1021/nl903946n

[45] Grzybowski, B. A.; Fitzner, K.; Paczesny, J.; Granick, S. From Dynamic Self-Assembly to Networked Chemical Systems. *Chem. Soc. Rev.* **2017**, *46*, 5647-5678, DOI: 10.1039/c7cs00089h.

[46] Gao, Y. G.; Kim, P. Y.; Hoagland, D. A.; Russell, T. P. Bidisperse Nanospheres Jammed on a Liquid Surface. *ACS Nano* **2020**, *14*, 10589-10599, DOI: 10.1021/acsnano.0c04682.

[47] Derrien, T. L.; Hamada, S.; Zhou, M.; Smilgies, D. M.; Luo, D. Three-Dimensional Nanoparticle Assemblies with Tunable Plasmonics Via a Layer-by-Layer Process. *Nano Today* **2020**, 30, DOI: 10.1016/j.nantod.2019.100823.

[48] Lee, D. W.; Min, Y. J.; Dhar, P.; Ramachandran, A.; Israelachvili, J. N.; Zasadzinski, J. A. Relating Domain Size Distribution to Line Tension and Molecular Dipole Density in Model Cytoplasmic Myelin Lipid Monolayers. *Proc. Natl. Acad. Sci. U. S. A.* **2011**, 108, 9425-9430, DOI: 10.1073/pnas.1106368108.

[49] Kim, P. Y.; Fink, Z.; Zhang, Q. T.; Dufresne, E. M.; Narayanan, S.; Russell, T. P. Relaxation and Aging of Nanosphere Assemblies at a Water-Oil Interface. *ACS Nano* **2022**, *16*, 8967-8973, DOI: 10.1021/acsnano.2c00020.

[50] Atkinson, S.; Stillinger, F. H.; Torquato, S. Existence of Isostatic, Maximally Random Jammed Monodisperse Hard-Disk Packings. *Proc. Natl. Acad. Sci. U. S. A.* **2014**, *111*, 18436-18441, DOI: 10.1073/pnas.1408371112.

[51] Draine, B. T.; Flatau, P. J. Discrete-Dipole Approximation for Periodic Targets: Theory and Tests. *J. Opt. Soc. Am. A* **2008**, 25, 2693-2703, DOI: 10.1364/Josaa.25.002693.

[52] Yang, G.; Kim, K.; Wang, W. T.; Chen, B. H.; Mattoussi, H.; Hallinan, D. T. Scaling Laws for Polymer Chains Grafted onto Nanoparticles. Macromol. *Chem. Phys.* **2018**, 219, DOI; 10.1002/macp.201700417.

[53] Mohammed, S.; Asgar, H.; Kuzmenko, I.; Gadikota, G. Self-Assembly of Silica Nanoparticles at Water-Hydrocarbon Interfaces: Insights from in Operando Small-Angle X-Ray Scattering Measurements and Molecular Dynamics Simulations. *Energy Fuels* **2020**, 34, 12545-12555, DOI: 10.1021/acs.energyfuels.0c02759.

[54] Hanrath, T.; Choi, J. J.; Smilgies, D. M. Structure/Processing Relationships of Highly Ordered Lead Salt Nanocrystal Superlattices. *ACS Nano* **2009**, 3, 2975-2988, DOI: 10.1021/nn901008r.

[55] Kostiainen, M. A.; Ceci, P.; Fornara, M.; Hiekkataipale, P.; Kasyutich, O.; Nolte, R. J. M.; Cornelissen, J. J. L. M.; Desautels, R. D.; van Lierop, J. Hierarchical Self-Assembly and Optical Disassembly for Controlled Switching of Magnetoferritin Nanoparticle Magnetism. *ACS Nano* **2011**, 5, 6394-6402, DOI: 10.1021/nn201571y.

[56] Li, T.; Senesi, A. J.; Lee, B. Small Angle X-Ray Scattering for Nanoparticle Research. *Chem. Rev.* **2016**, *116*, 11128-11180, DOI: 10.1021/acs.chemrev.5b00690.

[57] Veschgini, M.; Abuillan, W.; Inoue, S.; Yamamoto, A.; Mielke, S.; Liu, X. H.; Konovalov, O.; Krafft, M. P.; Tanaka, M. Size, Shape, and Lateral Correlation of Highly Uniform, Mesoscopic, Self-Assembled Domains of Fluorocarbon-Hydrocarbon Diblocks at the Air/Water Interface: A Gisaxs Study. *Chemphyschem* **2017**, *18*, 2791-2798, DOI: 10.1002/cphc.201700325.

[58] Yin, W.; Dadmun, M. A New Model for the Morphology of P3ht/Pcbm Organic Photovoltaics from Small-Angle Neutron Scattering: Rivers and Streams. *ACS Nano* **2011**, 5, 4756-4768, DOI: 10.1021/nn200744q.

[59] Krejci, A. J.; Thomas, C. G. W.; Mandal, J.; Gonzalo-Juan, I.; He, W. D.; Stillwell, R. L.; Park, J. H.; Prasai, D.; Volkov, V.; Bolotin, K. I.; Dickerson, J. H. Using Voronoi Tessellations to Assess Nanoparticle-Nanoparticle Interactions and Ordering in Monolayer Films Formed through Electrophoretic Deposition. *J. Phys. Chem. B* **2013**, 117, 1664-1669, DOI: 10.1021/jp305958w.

[60] Kim, P. Y.; Gao, Y. G.; Fink, Z.; Ribbe, A. E.; Hoagland, D. A.; Russell, T. P. Dynamic Reconfiguration of Compressed 2D Nanoparticle Monolayers. *ACS Nano* **2022**, 16, 5496-5506, DOI: 10.1021/acsnano.1c09853.

[61] Brock, J. D.; Strandburg, K. J.; Bond-Orientational Order. In *Bond-Orientational Order in Condensed Matter Systems*; Strandburg, K. J. Ed. Springer US, **2012**, pp 1-77.

[62] Volkert, A. A.; Subramaniam, V.; Ivanov, M. R.; Goodman, A. M.; Haes, A. J. Salt-Mediated Self-Assembly of Thioctic Acid on Gold Nanoparticles. *ACS Nano* **2011**, 5, 4570-4580, DOI: 10.1021/nn200276a.

[63] Kim, P. Y.; Ribbe, A. E.; Russell, T. P.; Hoagland, D. A. Visualizing the Dynamics of Nanoparticles in Liquids by Scanning Electron Microscopy. *ACS Nano* **2016**, 10, 6257- 6264, DOI: 10.1021/acsnano.6b02432.

**TOC:**

The assembly of mixed plasmonic and non-plasmonic nanoparticles are characterized using UV-Vis reflection spectroscopy, GISAXS, and SEM. Small gold NP clusters form quickly, while NP rearrangements at later times allow for additional NP recruitment and subsequent ordering within the domain. Gold NP domains coarsen over time, but mixtures with intermediate non-plasmonic content exhibited spectral narrowing, indicating an increase in order.